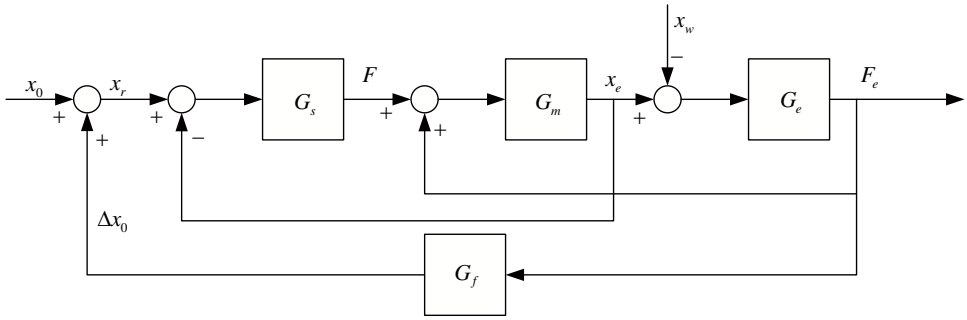


Figure 3.9: Block diagram of the position-based impedance control scheme

From eq. 3.40 to ensure the desired impedance characteristics

$$G_f = G_p^{-1} G_d - G_s^{-1} \tag{3.42}$$

For contact problem, without loss of generality, we may set the desired and static environment nominal positions to zero., i.e., $x_0 = 0, x_e = 0$. With these nominal values,

$$F = G_s(G_f F_e - X_e) \tag{3.43}$$

## Effect of Base Motion

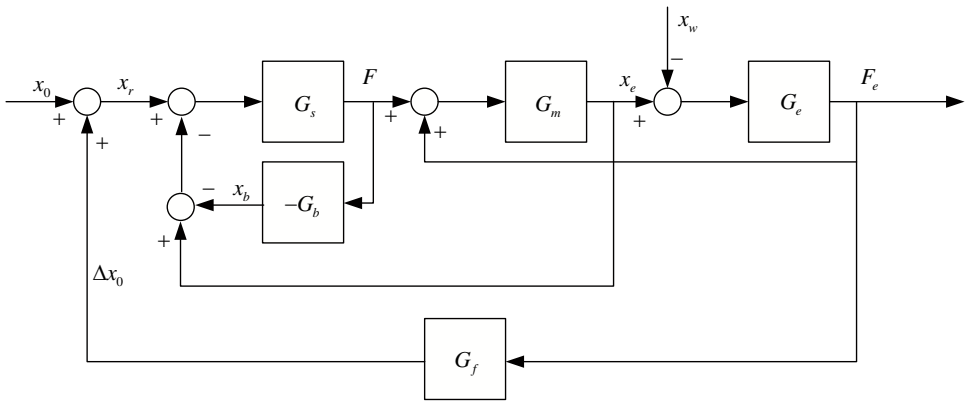


Figure 3.10: Block diagram of the position-based impedance control scheme in the FSMM

With the base motion, the measurement of the manipulator end-effector by on-board sensors is not $X_e$ but instead $X_e - X_b$. The block diagram of the position-

based impedance control in the FSMM is shown in fig. 3.10. Here,

$$\begin{aligned} F &= G_s(G_f F_e - X_e + X_b) \qquad (3.44)\\ &= G_s(G_f F_e - X_e - G_b F) \\ F &= (1 + G_s G_b)^{-1} G_s G_f F_e - (1 + G_s G_b)^{-1} G_s X_e \qquad (3.45) \end{aligned}$$

Substituting into the equation of motion

$$\begin{aligned} F + F_e &= G_m^{-1} X_e \\ (1 + G_s G_b)^{-1} G_s G_f F_e - (1 + G_s G_b)^{-1} G_s X_e + F_e &= G_m^{-1} X_e \\ G_s G_f F_e + (1 + G_s G_b) F_e &= G_s X + (1 + G_s G_b) G_m^{-1} X_e \end{aligned}$$

or

$$\begin{aligned} T_{pb} = \frac{X_e}{F_e} &= \frac{1 + G_s G_b + G_s G_f}{(1 + G_s G_b) G_m^{-1} + G_s} \\ &= G_m \frac{1 + G_s G_b + G_s G_f}{1 + G_s G_b + G_s G_m} \qquad (3.46) \end{aligned}$$

Substituting eq. 3.42 into equation above and rearranging yields

$$T_{pb} = G_m \frac{G_s G_b + G_s G_d + G_d G_m^{-1}}{1 + G_s G_b + G_s G_m} \qquad (3.47)$$

In the case where the transfer function between the force and end-effector displacement is modeled as a simple mass, i.e.,

$$G_m = \frac{1}{ms^2}$$

the transfer function in eq. 3.47 is given by

$$\begin{aligned} T_{pb} &= \frac{1}{ms^2} \frac{G_s G_b + G_s G_d + ms^2 G_d}{1 + G_s G_b + \frac{G_s}{ms^2}} \\ &= \frac{1}{ms^2} \frac{G_b + G_d + ms^2 G_s^{-1} G_d}{G_b + G_s^{-1} + \frac{1}{ms^2}} \\ &= \frac{1}{ms^2} \frac{G_b + \left(G_s^{-1} + \frac{1}{ms^2}\right) ms^2 G_d}{G_b + \left(G_s^{-1} + \frac{1}{ms^2}\right)} \qquad (3.48) \end{aligned}$$

Let

$$A = \frac{1}{ms^2 G_d} \qquad (3.49)$$

and

$$B = \left(G_s^{-1} + \frac{1}{ms^2}\right)^{-1} \qquad (3.50)$$

Then,

$$\begin{aligned} T_{pb} &= \frac{X_e}{F_e} = \frac{1}{ms^2}\frac{G_b + B^{-1}A^{-1}}{G_b + B^{-1}} \\ &= \frac{1}{ms^2}\frac{1 + BAG_b}{A + BAG_b} \end{aligned} \tag{3.51}$$

This equation is in a similar form to eq. 3.27 in the force-based control. Actually, for

$$G_d = Z_d^{-1} = \frac{1}{m_d s^2 + K}$$

eq. 3.49 becomes

$$A = \frac{m_d s^2 + K}{ms^2} = \frac{m_d}{m} + \frac{K}{ms^2}$$

which is the same as eq. 3.28. Thus,

$$\begin{aligned} BA &= \left(G_s^{-1} + \frac{1}{ms^2}\right)^{-1}\left(\frac{m_d}{m} + \frac{K}{ms^2}\right) \\ &= \frac{\frac{m_d}{m} + \frac{K}{ms^2}}{\frac{1}{G_s} + \frac{1}{ms^2}} \\ &= \frac{ms^2 G_s}{ms^2 + G_s}\frac{m_d s^2 + K}{ms^2} \\ &= \frac{G_s\left(m_d s^2 + K\right)}{ms^2 + G_s} \end{aligned} \tag{3.52}$$

In terms of $K$

$$BA = K\left(\frac{\frac{m_d}{mK} + \frac{1}{ms^2}}{\frac{1}{G_s} + \frac{1}{ms^2}}\right)$$

Therefore, if $G_s$ is selected such that

$$G_s = \frac{m}{m_d}K \tag{3.53}$$

then $BA \to K$. **In this case, the position-based impedance controller is equivalent to the force-based impedance controller**.

Similar to the force-based case, contact stability requires that

$$\angle\left(A(j\omega) + B(j\omega)A(i\omega)G_b(j\omega)\right) \neq \angle\left(1 + B(j\omega)A(i\omega)G_b(j\omega)\right), \quad \forall\omega > 0 \tag{3.54}$$

or similar to ineq. 3.31

$$\angle\left(A(j\omega) + e^{j\phi}g(\omega)\right) \neq \left(1 + e^{j\phi}g(\omega)\right), \quad \forall\omega > 0, \phi \tag{3.55}$$

for

$$|B(j\omega)A(j\omega)G_b(j\omega)| < g(\omega) \tag{3.56}$$

The uncertainty bound in this case is different from the one in the force-base case (in ineq. 3.30):

$$\begin{aligned} &\text{force-based:} && |K(j\omega)G_b(j\omega)| = |K(j\omega)|\,|G_b(j\omega)| \\ &\text{position-based:} && |B(j\omega)A(j\omega)G_b(j\omega)| = |B(j\omega)A(j\omega)|\,|G_b(j\omega)| \end{aligned}$$

**Designing $G_s$**

With high gain servo controller the uncertainty term $|B(j\omega)A(j\omega)G_b(j\omega)|$ can be much larger than $|K(j\omega)G_b(j\omega)|$ and will affect stability of the system. Consider a servo controller of the form

$$G_s = \alpha \frac{m}{m_d} K \tag{3.57}$$

where $\alpha$ is a scalar factor. For a passive function

$$K = b_d s + k_d$$

the servo controller is actually a PD controller. The form of $G(s)$ in eq. 3.57 deems appropriate as normally $K(s)$ would be designed to have good impedance behavior as would also be required for the servo controller. With this controller,

$$\begin{aligned} BA &= \frac{G_s\left(m_d s^2 + K\right)}{m s^2 + G_s} \\ &= \frac{\alpha \frac{m}{m_d} K\left(m_d s^2 + K\right)}{m s^2 + \alpha \frac{m}{m_d} K} \\ &= K \frac{\alpha\left(m_d s^2 + K\right)}{m_d s^2 + \alpha K} \end{aligned}$$

Then with $K(s) = b_d s + k_d$,

$$\begin{aligned} BA(j\omega) &= K(j\omega) \frac{(-\alpha m_d \omega^2 + \alpha k_d) + j\alpha b_d \omega}{(-m_d \omega^2 + \alpha k_d) + j\alpha b_d \omega} \\ |BA(j\omega)| &= |K(j\omega)| \left| \frac{(-\alpha m_d \omega^2 + \alpha k_d) + j\alpha b_d \omega}{(-m_d \omega^2 + \alpha k_d) + j\alpha b_d \omega} \right| \end{aligned}$$

The uncertainty bound of the position-based impedance controller will be greater than the uncertainty bound of the force-based impedance controller when

$$\begin{aligned} \left(-\alpha m_d \omega^2 + \alpha k_d\right)^2 &> \left(-m_d \omega^2 + \alpha k_d\right)^2 \\ \alpha^2 m_d^2 \omega^4 - 2\alpha^2 k_d m_d \omega^2 &> m_d^2 \omega^4 - 2\alpha m_d k_d \omega^2 \\ m_d \omega^2 \left(1 - \alpha^2\right) - 2\alpha k_d \left(1 - \alpha\right) &< 0 \\ m_d \omega^2 \left(1 + \alpha\right)\left(1 - \alpha\right) - 2\alpha k_d \left(1 - \alpha\right) &< 0 \end{aligned}$$

which can be divided into two cases according to the value of $\alpha$:

- $\alpha < 1 \Rightarrow \omega < \sqrt{2\frac{k_d}{m_d}\frac{\alpha}{\alpha+1}}$
- $\alpha > 1 \Rightarrow \omega > \sqrt{2\frac{k_d}{m_d}\frac{\alpha}{\alpha+1}}$

Figure 3.11 shows plots comparing the magnitudes $|K(j\omega)|$ and $|B(j\omega)A(j\omega)|$ for several values of $\alpha$. In general, for the servo controller we would expect to have $\alpha$ larger than 1. Therefore, in high frequency range the uncertainty bound of the position-based controller is expected to be larger than the uncertainty bound of the force-based controller. This will be critical if $|B(j\omega)A(j\omega)|$ is large in the frequency range close to natural frequencies of $G_b$.

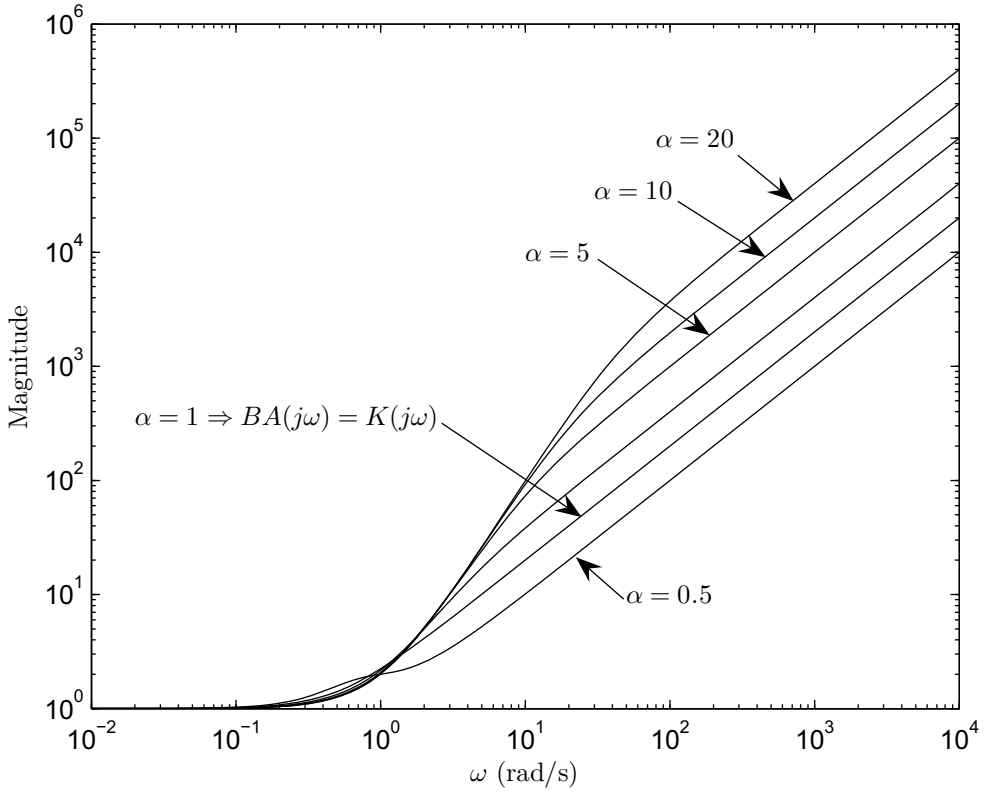


Figure 3.11: Plots of $|B(j\omega)A(j\omega)|$ (for $K(s) = 1.4s + 1, m_d = 1, m = 10, G_s = \alpha\frac{m}{m_d}K$ )

Figure 3.11 shows plots of $|B(j\omega)A(j\omega)G_b(j\omega)|$ for several values of $\alpha$ . The base is assumed to be a simple spring-mass-damper system with $m_b = 15$ kg, $b_b =$

300 N.s/m, $k_b$ = 37500 N/m which corresponds to a second order system with natural frequency 50 rad/s and damping ratio 0.2. The plot shows the magnitude of the bounds in which the greatest bound is at the natural frequency of the base. It is clearly seen that the larger the value of $\alpha$ the greater the uncertainty bound.

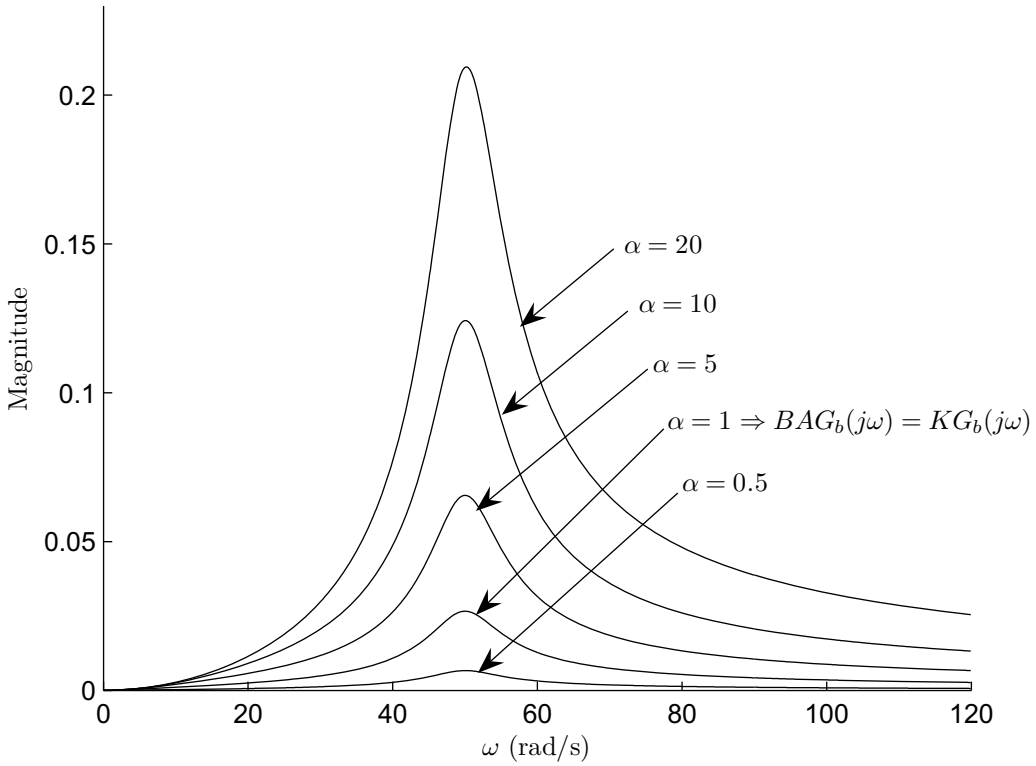


Figure 3.12: plots of $|B(j\omega)A(j\omega)G_b(j\omega)|$ (for $K(s) = 1.4s + 1, m_d = 1, m = 10, G_s = \alpha\frac{m}{m_d}K, G_b = \frac{1}{15s^2+300s+37500}$)

## Robust controller design

Consider the control law

$$F = G_s(G_f F_e - X + X_b)$$

with

$$G_f = G_p^{-1}G_d Q^{-1} - G_s^{-1} = \frac{1 + G_s G_m}{G_s G_m}G_d Q^{-1} - \frac{1}{G_s} \tag{3.58}$$

where $Q$ is an additional filter to be designed. With this control law, eq. 3.46 yields

$$\begin{aligned}
T_{pb} &= G_m \frac{1 + G_s G_b + G_s G_f}{1 + G_s G_b + G_s G_m} \\
&= G_m \frac{G_s G_b + \frac{G_d}{G_m} Q^{-1} + G_s G_d Q^{-1}}{1 + G_s G_b + G_s G_m} \\
&= \frac{1}{ms^2} \frac{G_s G_b + ms^2 G_d Q^{-1} + G_s G_d Q^{-1}}{1 + G_s G_b + \frac{G_s}{ms^2}} \\
&= \frac{1}{ms^2} \frac{G_b + G_d Q^{-1} + ms^2 G_s^{-1} G_d Q^{-1}}{G_b + G_s^{-1} + \frac{1}{ms^2}} \\
&= \frac{1}{ms^2} \frac{G_b + \left(G_s^{-1} + \frac{1}{ms^2}\right) ms^2 G_d Q^{-1}}{G_b + \left(G_s^{-1} + \frac{1}{ms^2}\right)} \\
&= \frac{1}{ms^2} \frac{G_b + B^{-1} A^{-1} Q^{-1}}{G_b + B^{-1}} \\
T_{pb} &= \frac{1}{ms^2} \frac{1 + BAQG_b}{AQ + BAQG_b}
\end{aligned} \tag{3.59}$$

The filter $Q$ can be designed such that the magnitude of its frequency response function is small in the range where $BAG_b$ is expected to be large, i.e. at the natural frequencies of $G_b$ and also to keep the angle $\theta = \angle(1 - A(j\omega)Q(j\omega))$ as close to 90° as possible of for wide range of $\omega$. Consider $Q$ in the form of a lag-compensator

$$Q(s) = \frac{\tau_1 s + 1}{\tau_2 s + 1}$$

with $\tau_1 < \tau_2$. Here, $|Q(j\omega)|$ will drops below 1 after the corner frequency $\omega_a = 1/\tau_2$ with the rate of $-20$ dB/decade and will remain constant after $\omega_b = 1/\tau_1$. We can select $\tau_2$ such that $\omega_a$ is less than the first natural frequency of the base. The lag compensator $Q$ will also help to keep the angle $\theta$ larger when $\omega$ increases, thus providing robustness. Figure 3.13 shows the comparison of the uncertainty bound with and without the filter at $\alpha = 20$. As seen in the figure, the uncertainty bound can be reduced substantially with $Q$.

Figure 3.14 shows the plots of $AQ(j\omega)$ compared to $A(j\omega)$ for $\omega = [1, 120]$ rad/s. Here the magnitude and phase of $A(j\omega)$ is reduced by the effect of the filter $Q$. The phase of $AQ(j\omega)$ approaches 0° less quickly as $\omega$ increases and therefore the system is more robust. Figure 3.15 shows the Nyquist plots of $T_{pb}$ with and without the filter $Q$. Note that the plot shown in the figure is an expanded

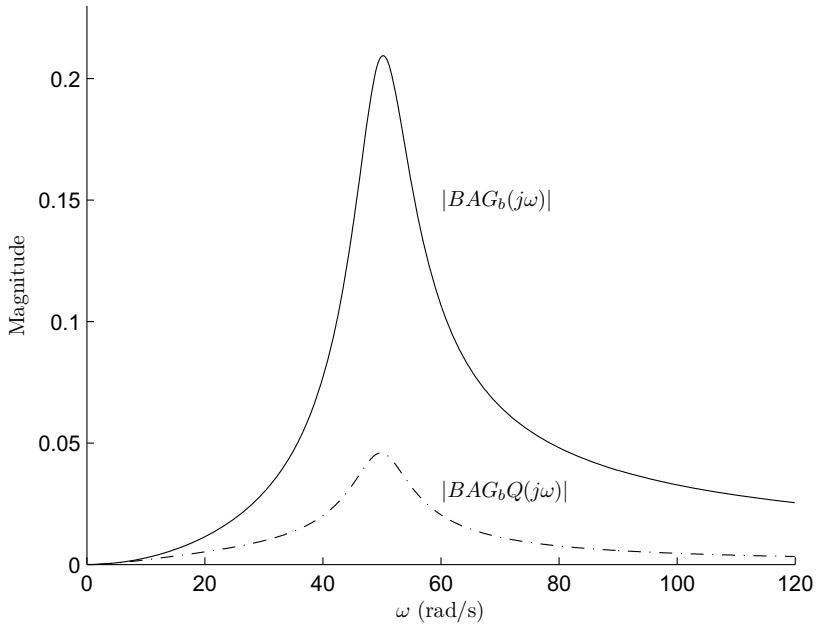


Figure 3.13: Comparison between the uncertainty bound with and without $Q$ (for $K(s) = 1.4s + 1, m_d = 1, m = 10, G_s = 20\frac{m}{m_d}K, G_b = \frac{1}{15s^2+300s+37500}, \tau_1 = 0.01, \tau_2 = 0.1$)

view only in high frequency range. Without the filter $Q$, the Nyquist plot crosses the negative real axis and therefore in contact with wall, the system can become unstable. With the filter $Q$, the Nyquist plot does not cross the negative real axis for the entire frequency range and therefore, provided that $T_{pb}$ is stable, the system is always stable in contact.

Although the filter $Q$ can be used to increase the robustness, it can effect the performance of the system. Therefore it should be designed taking in mind this aspect as well. As in the example above, the design of such $Q$ also gives good performance as shown fig. 3.16.

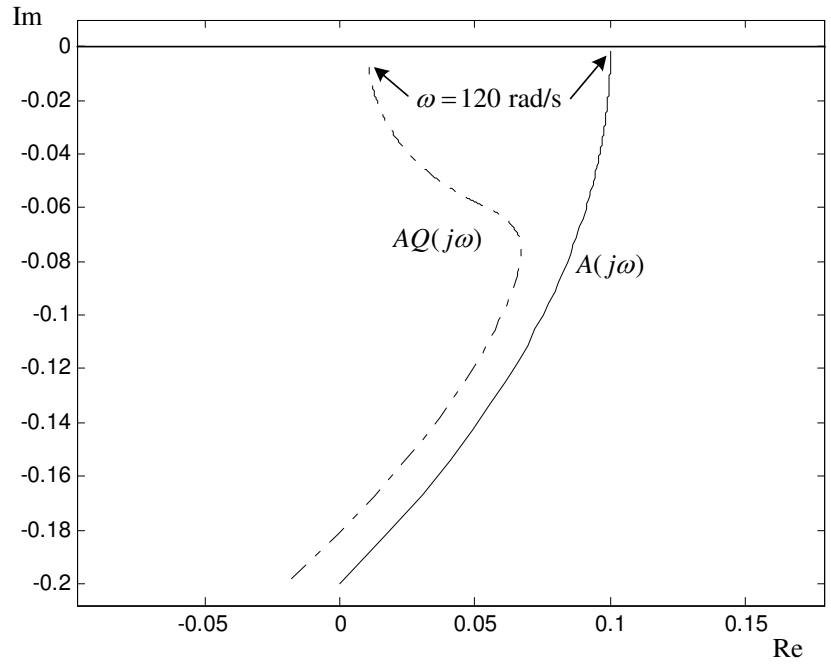


Figure 3.14: Plots of $A(j\omega)$ and $AQ(j\omega)$ (for $K(s) = 1.4s + 1, m_d = 1, m = 10, \tau_1 = 0.01, \tau_2 = 0.1$)

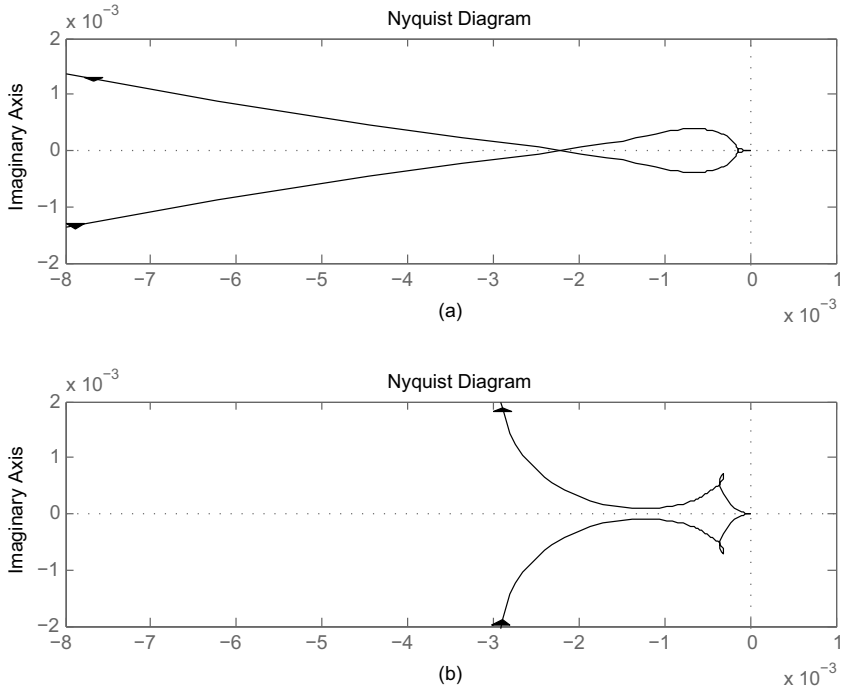


Figure 3.15: Nyquist plots of $T_{pb}$ – in high frequency range (a) without filter $Q$ (b) with filter $Q$ (for $K(s) = 1.4s + 1, m_d = 1, m = 10, G_s = 20\frac{m}{m_d}K, G_b = \frac{1}{15s^2+300s+37500}, \tau_1 = 0.01, \tau_2 = 0.1$)

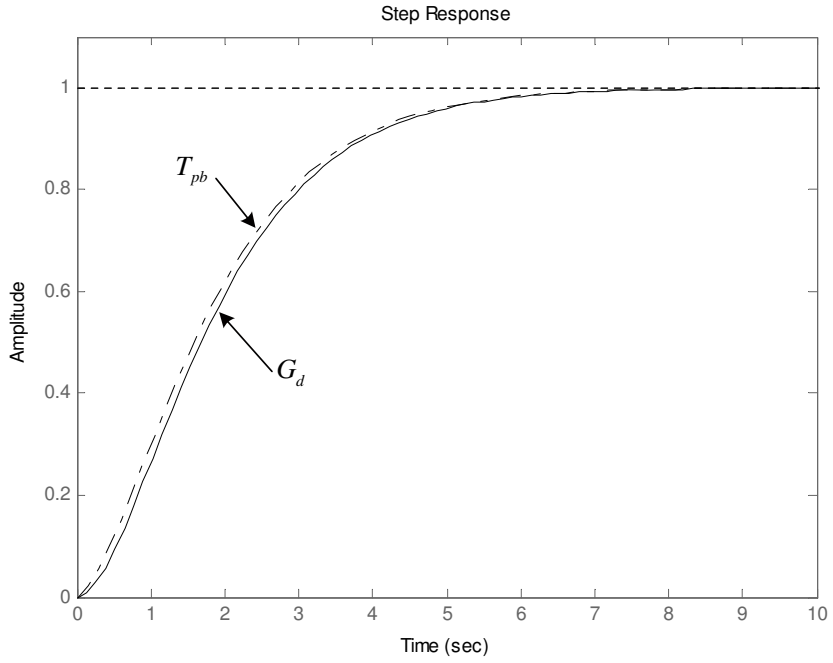


Figure 3.16: Step responses of: (solid) desired admittance $G_d$, (dash-dot) $T_{pb}$ with $Q$ (for $K(s) = 1.4s + 1, m_d = 1, m = 10, G_s = 20\frac{m}{m_d}K, G_b = \frac{1}{15s^2+300s+37500}, \tau_1 = 0.01, \tau_2 = 0.1$)

# Chapter 4

# Experimental Setup and Results

## 4.1 Experimental setup

### 4.1.1 A 2-DOF FSMM Test Rig

Figure 4.1 shows the drawing of a 2-DOF FSMM used for testing the control scheme. It composes of a rigid manipulator with two arms sitting on a platform which is made of a steel rectangular plate mounted, at its corners, to four long stainless poles. The first natural mode of vibration of the flexible structure is around 7 Hz. The arms of the manipulator travel on the horizontal plane and so is the vibration of the base. The manipulator arms are driven by d.c. motors through harmonic gear units. The angles of arm movement are measured by incremental encoders. Arm 1 has a counter mass attached to the opposite end to bring the center of mass closer to the arm joint. At the tip of arm 2, a six-axis force/torque sensor is installed to measure the force exerted by the wall during contact. Under the base, a two axis-accelerometer is installed to measure the base acceleration. The manipulator is installed near the wall so that the contact test can be performed. Figure 4.2 shows the picture of the 2-DOF FSMM that has been constructed and Table 4.1 lists the parameters of the system. The details and specifications of the sensors and motors are given in Appendix.

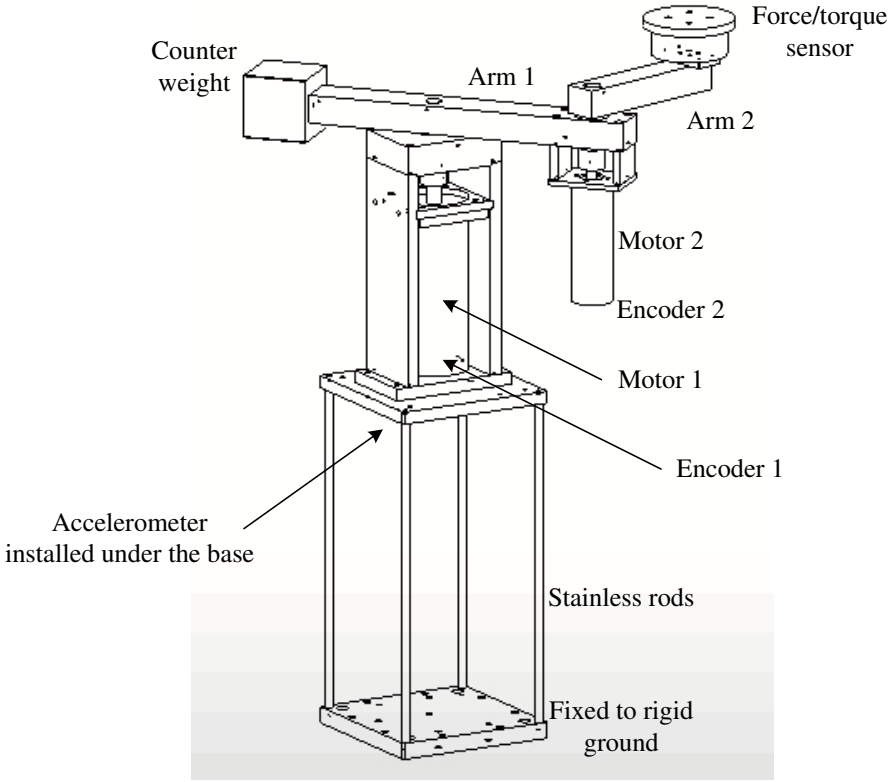


Figure 4.1: Drawing of a 2-DOF lab-scale FSMM

Figure 4.2: The 2-DOF lab-scale FSMM

Table 4.1: Parameters of the lab-scale FSMM

| Item | Parameter |
|---|---|
| mass of arm 1 | 6.97 kg |
| mass of arm 2 | 2.76 kg |
| moment of inertia of arm 1 (reference to c.m.) | 0.2262 kg.m$^2$ |
| moment of inertia of arm 2 (reference to c.m.) | 0.0098 kg.m$^2$ |
| mass of the base | 11.97 kg |
| length of arm 1 | 0.202 m |
| length of arm 2 | 0.1625 m |
| center of mass of arm 1 (measured from arm joint) | 0.0524 m |
| center of mass of arm 2 (measured from arm joint) | 0.1288 m |

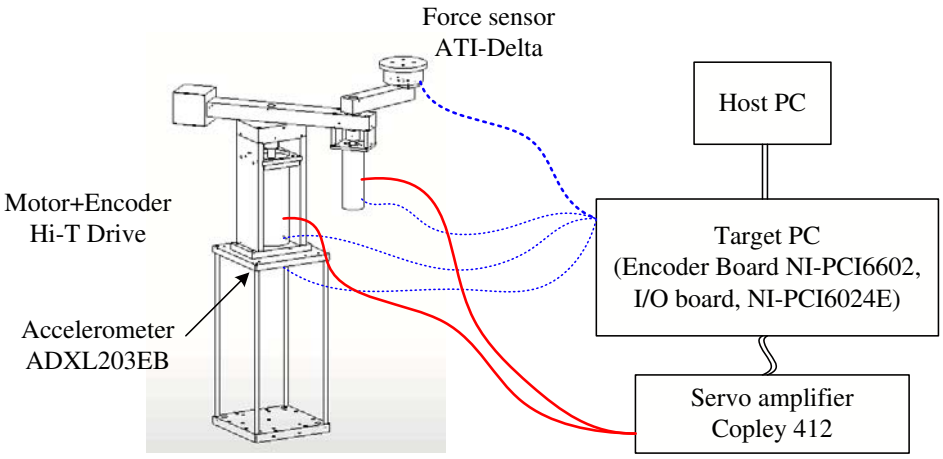


Figure 4.3: Experimental setup

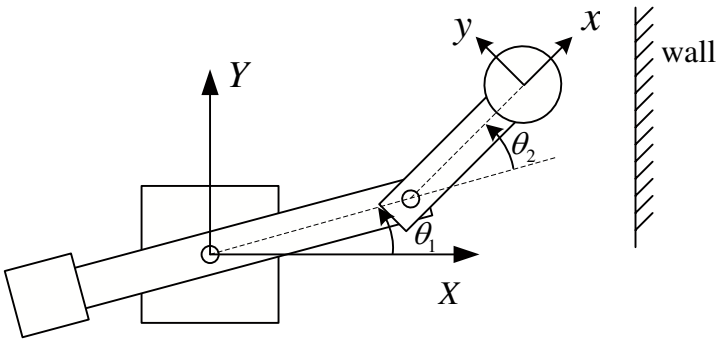


Figure 4.4: Coordinates of the FSMM

### 4.1.2 Experimental Setup

of

Figure 4.3 shows the diagram of the experimental setup. The control signal voltages are sent to the amplifiers which then supply the current proportional to the control signal to the motors. The sensors installed are as follows: 1) the encoders measure the angles of of rotation of the arms and send the signal to the encoder board installed in the computer 2) the force sensor measures the force exerted on the end-effector and sends the force signal to the I/O board also installed in the computer 3) the accelerometer measures the acceleration of the manipulator base and sends acceleration signals to the I/O board. The real-time signal is generated by the xPc Target system with MATLAB, Simulink and Real-Time-Workshops. The coordinates of manipulator base and the end-effector are defined corresponding to the diagram in fig. 4.4. Note that the wall has the surface normal vector in the direction opposite to the positive $X$ axis.

### 4.1.3 Test Procedure

In order to test the performance of the control system, contact tests were performed. In the test, the end-effector of the manipulator was set up to initially touch the wall by giving an end-point reference command slightly inside the wall. The contact force and acceleration signals in the $X$-direction were then observed.

## 4.2 Results

### 4.2.1 Force-based control

In this experiment, many tests were performed for various sets of desired impedance parameters. The aim was to look for the conditions where unstable contacts can be observed and see how the robust controller can improve the stability. In some cases, the impedance controller could provide stable contact without $Q(s)$. And in other cases, the system were unstable. An example of the case where unstable contact occurs is when the desired impedance is set to $m_d = 50, b_d = 439.8, k_d = 1974.0$. Figure 4.5 shows the acceleration and contact force signals when the end-effector made contact with the wall. Here, mild vibrations in the system could be visually observed but the end-effector was still in contact with the wall. These vibrations can also be observed from the contact force signal with the amplitude fluctuating around $\pm$2.5N. In this case the system is unstable. Figure 4.6 shows the acceleration and contact force signals of another set up where the system was initially unstable as can be seen from fluctuation in the contact force signal. At time $t = 1$ second, $Q(s) = \frac{0.1s+1}{0.01s+1}$ was added to the controller. With $Q(s)$, the vibration in the system died out quickly and after a few second, the system settled down. Figure 4.7 shows the step responses of the system with impedance controller with $Q(s)$. The end-effector was initially set to contact the wall and had stable contact. At time $t = 1$ second, a step command was given so that the end-effector moved further into the wall. After the step command, the end-effector firstly reacted as if it would move out of the wall, but quickly it moved back into the wall and settled down with no vibration. From these plots, it is clear that $Q(s)$ improves stability of the system.

### 4.2.2 Position-based control

In this experiment, many tests were performed for various sets of desired impedance parameters and servo control parameters. In some cases, the impedance controller could provide stable contact without $Q(s)$. And in other cases, the system were unstable. An example of the case where unstable contact occurred is shown be-

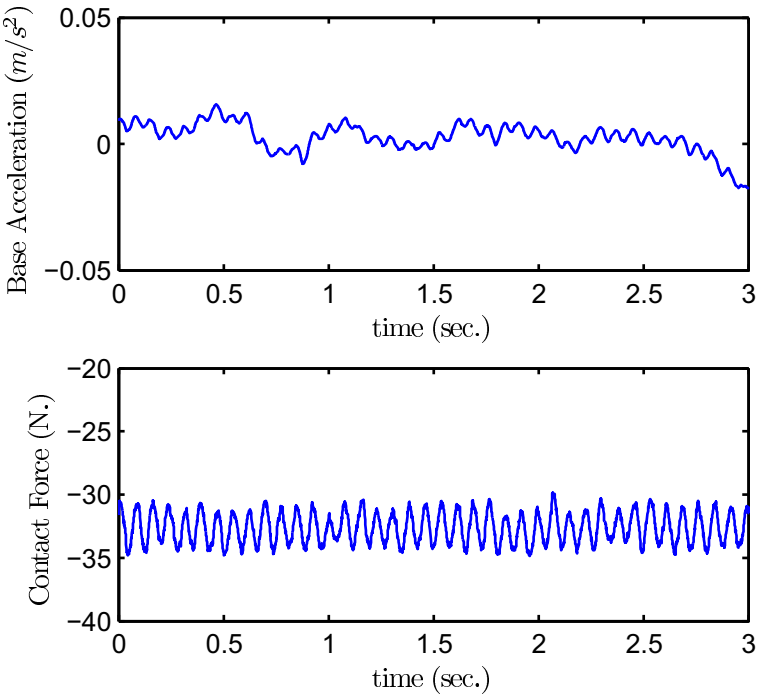


Figure 4.5: The plots of acceleration and contact force for the system with force-based impedance control shows unstable contact (no $Q(s)$ applied): $m_d = 50, b_d = 439.8, k_d = 1974.0$

low. Here, the desired impedance parameters were set to $m_d = 20, b_d =, k_d = 439.82, k_d = 3947.8$ which correspond to the spring-mass-damper system with natural frequency 2 Hz and damping ratio 0.7. The servo controller is a PD controller with $b_s = 560.3, k_s = 25148$ which correspond to $\alpha$ in eq. 3.57 being about 25. In the test, the manipulator's end-effector was set to initially touch the wall with some contact force. Then, at time $t = 1$ second the manipulator was given a step command on the end-effector position. The end-effector new set-point position was further inside the wall to create more contact force. Figure 4.8 shows the plots of the base acceleration and contact force signals. Initially, the contact force acting on the end-effector is about 17 N. After the step command, large vibration (visibly observable) occurred in the system as can be observed in the base acceleration and the contact force signals. At time $t = 6.2$ second, the filter $Q(s) = \frac{0.1s+1}{0.01s+1}$ was added to the controller. With $Q(s)$, the vibration disappeared quickly.

Figure 4.9 shows the step response for the case where $Q(s)$ was included from

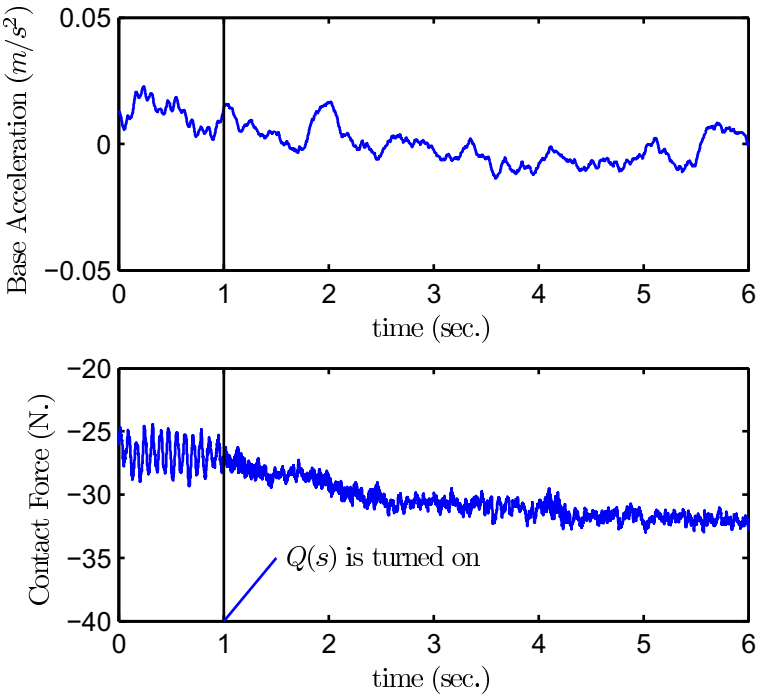


Figure 4.6: The plots of acceleration and contact force for the system with force-based impedance control shows stable contact after $Q(s)$ is applied : $m_d = 50, b_d = 439.8, k_d = 1974.0, Q = (0.01s + 1)/(0.1s + 1)$

the beginning. As can be observed, no vibration occurred in this case. Clearly, with $Q(s)$ the stability of the system is improved.

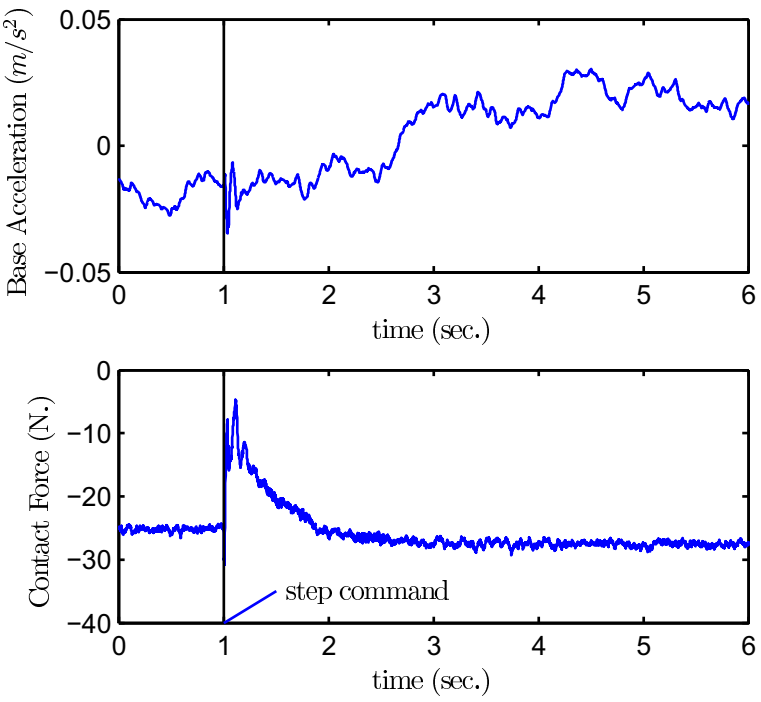


Figure 4.7: Step responses of the system with force-based impedance control with $Q(s)$ : $m_d = 50, b_d = 439.8, k_d = 1974.0, Q = (0.01s + 1)/(0.1s + 1)$

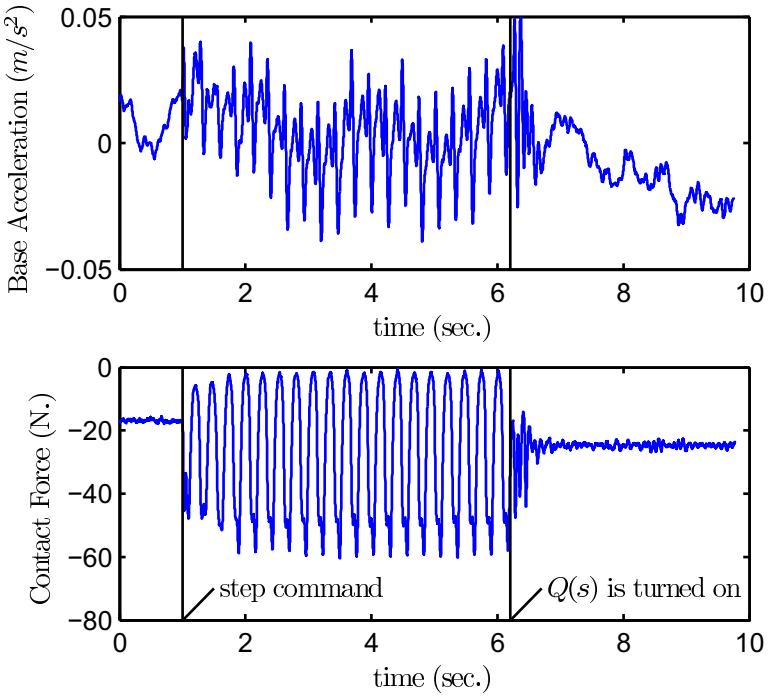


Figure 4.8: Step responses of the system with position-based impedance controller: $m_d = 25, b_d = 439.82, k_d = 3947.8, G_s = 560.3s+25148, Q(s) = (0.01s+1)/(0.1s+1)$

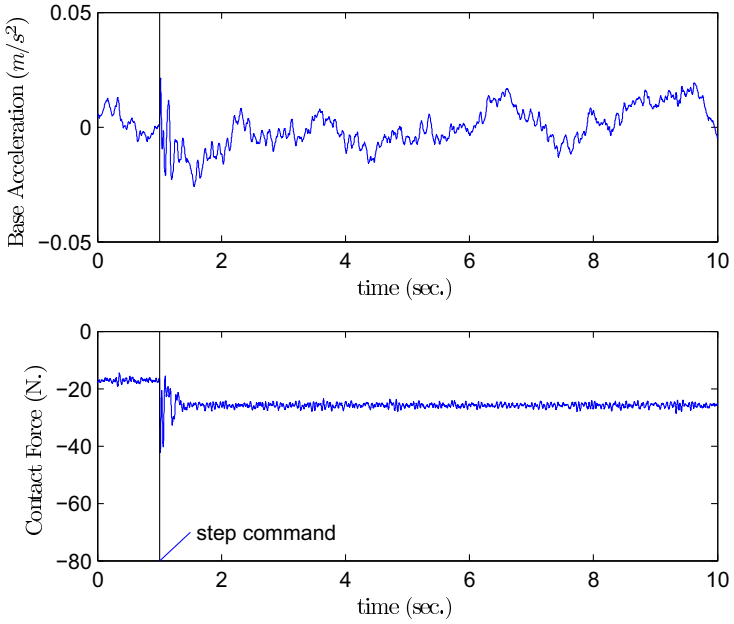


Figure 4.9: Step responses of the system with robust position-based impedance controller: $m_d = 25, b_d = 439.82, k_d = 3947.8, G_s = 560.3s + 25148, Q(s) = (0.01s + of1)/(0.1s + 1)$

# Chapter 5

# Conclusions

This research investigates force control techniques for flexible structure mounted manipulators performing contact tasks. Impedance control is the main subject of investigation. Two types of impedance control are studied: 1) force-based impedance control and 2) position-based impedance control. One-DOF contact model, along the surface normal direction, has been established. Based on the one-DOF model, the robust control schemes for both types of impedance control are derived. The goal is for the system to perform according to the desired impedance while remain stable when in contact with static environment such as wall. Based on the Nyquist stability criteria, the controllers are derived by ensuring that the Nyquist plots of the admittance of the controlled system do not cross the negative real axis. In order to verify the control schemes, a 2-DOF lab-scale flexible structure mounted manipulator has been constructed. Tests have been performed and the results show that the robust controllers can resolve the stability problems that occur under some conditions when non-robust controller are employed.

Although the controllers derived in this study can provide stable contact, the criteria employed are still conservative and therefore the contact performance may not be at its best. For further work, the robust performance during contact should be the main subject of study. Other issues such as joint flexibility, dynamic environment and friction should also be explored.

# Bibliography


[1] D. S. Kwon, D. H. Hwang, S. M. Babcock and B. L. Burks, "Input shaping filter methods for the control of structurally flexible, long-reach manipulators," Proceedings of the 1994 IEEE International Conference on Robotics and Automation, San Diago, May 1993

[2] J. Y. Lew, "Contact control of flexible micro/macro manipulators," Proceedings of the 1997 IEEE International conference on robotics and automation, Albuquerque, New Mexico, April 1997

[3] J. Y. Lew and D.J. Trudnowski, "Vibration control of a micro/macro manipulator system," IEEE control system magazine, February 1996

[4] - D. P. Magee and W. J. Book, "Filtering schilling manipulator commands to prevent flexible structure vibration," Proceedings of the American Control Conference, Baltimore 1994

[5] - D. N. Nenchev, K. Yoshida and M. Uchiyama, "Reaction null-space based control of flexible structure mounted manipulator systems," Proceedings of the 35th Conference on Decision and Control, Kobe, Japan, Dec 1996

[6] - J. R. Sagli and O. Egeland, "Using momentum conservation to control linematically redundant manipulators," Modeling, Identification and Control, Vol 12 n.1, 1991

[7] - M. A. Scott and M. G. Gilbert "Active vibration damping of the space shuttle remote manipulator system," Journal of Guidance, Control and Dynamics, Vol. 16 n. 2, 1993

[8] - I. Sharf, "Active damping of a large flexible manipulator with short-reach robot," Journal of Dynamic Systems, Measurement and Control, Vol. 118, Dec 1996

[9] - M. A. Torres and S. Dubowsky, "Path-planning for elastically constrained space manipulator systems," Proceedings of the 1993 IEEE International Conference on Robotics and Automation, Atlanta GA, May 1993

[10] - M. A. Torres, S. Dubowsky and A. C. Pisoni, "Path planning for elastically-mounted space manipulators: experiment evaluation," Proceedings of the 1994 IEEE Internal Conference on Robotic and Automation, San Diago, CA, May 1994

[11] - K. Yoshida, D.N. Nenchev, and M. Uchiyama, "Vibration suppression and zero reaction maneuvers of flexible space structure mounted manipulators," Smart Materials and Structures, Vol. 8, 1999

# Outputs

The results of this research work help to understand the theory outlining the impedance control of a flexible structure mounted manipulator performing contact tasks. The author has been writing an article to submit to an academic journal. The title of the article will be "Robust impedance controls for flexible structure mounted manipulator performing contact tasks". The writing of the article should be finished within two months from the date posted in this report.

# Appendix A

# Specifications of Sensors and Actuators

Table A.1: Specifications of Force Sensors

| **Item** | **Details** | |
|---|---|---|
| Made | ATI INDUSTRIAL AUTOMATION | |
| Model | Delta US-150-600 | |
| Sensing ranges | | |
| $F_x$, $F_y$ (±N) | 660 | |
| $F_z$ (±N) | 1,980 | |
| $T_x$, $T_y$ (±N-m) | 60 | |
| $T_z$ (±N-m) | 60 | |
| Resolution | Controller F/T System | 16 bit DAQ F/T System |
| $F_x$, $F_y$ (±N) | 1/2 | 1/32 |
| $F_z$ (±N) | 1 | 1/16 |
| $T_x$, $T_y$ (±N-m) | 3/100 | 3/1,600 |
| $T_z$ (±N-m) | 3/100 | 3/1,600 |
| Single-axis overload | | |
| $F_x$, $F_y$ (±N) | 3,400 | |
| $F_z$ (±N) | 12,000 | |
| $T_x$, $T_y$ (±N-m) | 220 | |
| $T_z$ (±N-m) | 420 | |
| Resonant frequency | | |
| $F_x, F_y, T_z$ | 1,500 Hz | |
| $F_z, T_x, T_y$ | 1,700 Hz | |
| Physical specifications | | |
| Weight | 910 g | |
| Diameter | 94.5 mm | |
| Height | 33.3 mm | |
| Temperature Error (from 22°C) | Typical gain error | |
| ±5°C | 0.1% | |
| ±15°C | 0.5% | |
| ±25°C | 1% | |
| ±50°C | 5% | |

Table A.2: Motor Specifications

| **Item** | **Motor 1** | **Motor 2** |
|---|---|---|
| Made | Harmonic Drive | Harmonic Drive |
| | System Inc. | System Inc. |
| Model | RH-20-3004-OEM | RH-14GH11OEM |
| Rate output power (W) | 90 | 20.3 |
| Rate current (A) | 3 | 1.8 |
| Peak current (A) | 15 | 5.4 |
| Torque constant (Nm/A) | 18.121 | 2.602 |
| Moment of inertia (kg.m$^2$) | 0.000026 (armature) | 0.0021 |
| Weight with encoder (kg) | 3.02 | 0.78 |
| Gear ratio | 1/100 | 1/50 |
| Encoder | | |
| Resolution (ppr) | 1,000 | 1,000 |
| Output signal | A, A/, B, B/, Z, Z/ | A, B, Z, |
| Power supply (VDC) | +5V TTL open collector | +5V TTL open collector |
| Max.output current (mA) | 20 | 20 |
| Max. signal freq. (kHz) | 100 | 100 |

Table A.3: Specifications of accelerometer

| **Item** | **Specification** |
|---|---|
| Made | Analog Devices |
| Model | ADXL203EB |
| No. of Axis | 2 |
| Range | ±1.7g |
| Sensitivity | 1000 mV/g |
| Sensitivity accuracy | ±6 |
| Output type | Analog |
| Bandwidth | 2.5 kHz |
| Noise density | 110 |
| Supply current | 0.7 mA |
| Supply voltage | 3 to 6 VDC |
| Temp range | -40°C to 125°C |
| Package | E-8 |